

SAM-Assisted Remote Sensing Imagery Semantic Segmentation with Object and Boundary Constraints

Xianping Ma, Qianqian Wu, Xingyu Zhao, Xiaokang Zhang, Man-On Pun, and Bo Huang

Abstract—Semantic segmentation of remote sensing imagery plays a pivotal role in extracting precise information for diverse downstream applications. Recent development of the Segment Anything Model (SAM), an advanced general-purpose segmentation model, has revolutionized this field, presenting new avenues for accurate and efficient segmentation. However, SAM is limited to generating segmentation results without class information. Consequently, the utilization of such a powerful general vision model for semantic segmentation in remote sensing images has become a focal point of research. In this paper, we present a streamlined framework aimed at leveraging the raw output of SAM by exploiting two novel concepts called SAM-Generated Object (SGO) and SAM-Generated Boundary (SGB). More specifically, we propose a novel object loss and further introduce a boundary loss as augmentative components to aid in model optimization in a general semantic segmentation framework. Taking into account the content characteristics of SGO, we introduce the concept of object consistency to leverage segmented regions lacking semantic information. By imposing constraints on the consistency of predicted values within objects, the object loss aims to enhance semantic segmentation performance. Furthermore, the boundary loss capitalizes on the distinctive features of SGB by directing the model’s attention to the boundary information of the object. Experimental results on two well-known datasets, namely ISPRS Vaihingen and LoveDA Urban, demonstrate the effectiveness of our proposed method. The source code for this work will be accessible at <https://github.com/sstary/SSRS>.

Index Terms—Remote Sensing, Semantic Segmentation, SAM, Object Loss, Boundary Loss

I. INTRODUCTION

Semantic segmentation of remote sensing imagery entails assigning semantic labels to individual pixels within images captured by various remote sensing sensors. This process is fundamental for diverse downstream geoscience applications, including environmental monitoring [1], land cover mapping [2], and disaster management [3, 4]. The primary objective is to accurately partition the image into distinct regions

This work was supported in part by the National Natural Science Foundation of China under grant 41801323, China Postdoctoral Science Foundation under grant 2020M682038 and the Shenzhen Science and Technology Innovation Committee under Grant No. JCYJ20190813170803617. (*Corresponding author: Man-On Pun, Xiaokang Zhang*)

Xianping Ma, Qianqian Wu, Xingyu Zhao and Man-On Pun are with the School of Science and Engineering, The Chinese University of Hong Kong, Shenzhen, Shenzhen 518172, China (e-mails: xianpingma@link.cuhk.edu.cn; qianqianwu@link.cuhk.edu.cn; xzhao911@usc.edu; SimonPun@cuhk.edu.cn).

Xiaokang Zhang is with the School of Information Science and Engineering, Wuhan University of Science and Technology, Wuhan 430081, China, and also with the Department of Land Surveying and Geo-Informatics, The Hong Kong Polytechnic University, Hong Kong, China.(e-mail: natezhangxk@gmail.com).

Bo Huang is with the Department of Geography, The University of Hong Kong, Hong Kong, SAR 999077, China (e-mail: hbcuhk@gmail.com).

representing different semantic classes, facilitating automated analysis and interpretation of remote sensing data. The advent of deep learning techniques [5, 6, 7, 8] has ushered in numerous high-performance, problem-specific methods in this field. According to the type of network, these methods can be primarily categorized into convolutional neural network (CNN) [9, 10, 11], transformer-based approaches [12, 13] and hybrid architecture [14, 15, 16, 17] for remote sensing applications.

Recently, a notable foundation model called Segment Anything Model (SAM) [18] designed for image segmentation gains considerable attention from the computer vision community. Trained on an extensive dataset of 11 million natural images and over one billion masks, SAM distinguishes itself by enabling zero-shot segmentation of new visual objects without prior exposure to them. As the first foundation model for general image segmentation, SAM and its original paper have garnered over 1000 citations within six months according to the google scholar website. However, two conspicuous limitations hinder the application of SAM to remote sensing image semantic segmentation tasks. Firstly, the generated segmentation masks lack semantic labels. Secondly, due to the disparities between natural images and remote sensing images, SAM’s effectiveness in remote sensing tasks is compromised [19].

To address these limitations and enhance SAM’s performance in remote sensing semantic segmentation tasks, researchers have explored various methods from different perspectives. These approaches include adapting or enhancing SAM [20, 21, 22], employing few-shot or zero-shot learning strategies [23, 24, 25, 26] and leveraging prompt learning techniques [27, 28, 29, 30, 31]. In particular, SAM-CD [21] directly utilizes FastSAM [32] to extract image features while incorporating the underlying temporal constraints in remote sensing images for change detection supervision. RS-CLIP [24] employs a curriculum learning strategy to boost the performance of zero-shot classification of remote sensing images using SAM through multiple stages of model finetuning. SAMRS [28] efficiently generates a large-scale remote sensing segmentation dataset by employing various prompts, thereby significantly expanding existing remote sensing datasets. However, these methods often necessitate the artificial design of complex fine-tuning mechanisms or prompt learning strategies. The former involves modifying the structures of the general semantic segmentation model and training strategies, while the latter requires specific prompts tailored to different datasets. Unfortunately, these factors impede the seamless integration of SAM into the field of remote sensing.

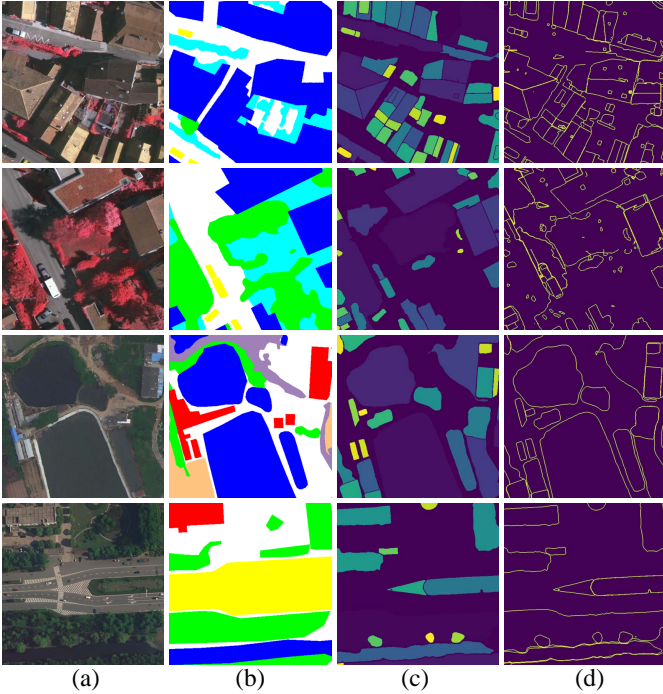


Fig. 1. Visual examples. (a) Images, (b) Ground truth, (c) SGO, (d) SGB. The first two rows show samples of size 512×512 from ISPRS Vaihingen. The last two rows show samples of size 1024×1024 from LoveDA Urban. It can be observed that SGO and SGB provide a wealth of detailed information about ground objects from both object and boundary perspectives.

To cope with the aforementioned challenges, we develop a simple yet effective framework to utilize SAM from the perspectives of both objects and boundaries. Our observations reveal that SAM encounters challenges in accurately segmenting remote sensing images due to disparities between remote sensing images and natural images. Nevertheless, SAM exhibits proficiency in recognizing *objects*, as evident in Fig. 1. It shows that SAM-Generated Object (SGO) and SAM-Generated Boundary (SGB) can provide detailed object and boundary information. To fully leverage their potential while minimizing modifications to the general semantic segmentation model, we propose a novel loss function, namely object loss and further introduce a boundary loss to aid in model training.

For the object loss, it is observed that the regions in SGO as shown in Fig. 1(c) are actually objects without semantic information. This insight motivates the design of the object loss, aiming to ensure consistency within a segmented object. Furthermore, we introduce the boundary loss [33] to encourage the segmentation model to better consider segment boundaries based on the detailed SGB information. As both loss functions take the semantic segmentation output from the general segmentation model as inputs, there is no need for additional segmentation heads at the tail of the decoder. By harnessing a simple and direct utilization of SGO and SGB, the foundational visual knowledge embedded in SAM contributes to enhancing the semantic segmentation performance of remote sensing images. This approach holds the potential for direct implementation across various tasks involving the combination

of SAM and remote sensing. The contributions of this work can be summarized as follows:

- We have developed a streamlined framework that efficiently leverages two novel concepts called SGO and SGB for remote sensing segmentation, which underscores the value and effectiveness of the *raw* output of SAM. Notably, our approach distinguishes itself by not necessitating specific designs for the model, training strategy, or pseudo-label generation, in contrast to other existing SAM-based methods employed in remote sensing;
- We propose a novel object loss and further introduce the boundary loss to assist with model optimization, making full use of the raw output of SAM. This is achieved without relying on semantic information, focusing on two crucial perspectives: object and boundary. To our best knowledge, the object loss is the first method in semantic segmentation tasks that can directly utilize the raw output of SAM without the need for additional class prompts;
- Extensive experiments on two well-known, publicly available remote sensing datasets, ISPRS Vaihingen and LoveDA Urban, confirm that the proposed approach can be widely adapted to semantic segmentation tasks of different datasets and different models. We believe that this approach has the potential to significantly expand the application of SGO and SGB, unlocking the full capabilities of large models like SAM in remote sensing semantic segmentation tasks.

The remainder of this paper is organized as follows. Sec. II first reviews the related works of SAM in different fields. After that, Sec. III presents the proposed method in detail, whereas Sec. IV provides experimental results and discussions. Finally, the conclusion is given in Sec. V.

II. RELATED WORKS

A. Segment Anything Model

The Segment Anything Model (SAM), introduced by Meta AI [34], is a large vision transformer [8]-based model trained on a substantial visual corpus. It is a foundation model aiming to address specific downstream image segmentation tasks. One of the challenges in applying deep neural networks to real-world semantic segmentation applications, is the need for large amounts of well-annotated training data. SAM is an effective tool to address this issue by enabling zero-shot generalization to *unseen* images and objects based on user-provided prompts. The framework of SAM has three main components, namely an image encoder, a prompt encoder, and a mask decoder. The image encoder utilizes a vision transformer-based approach for extracting image features. The prompt encoder incorporates user interactions for segmentation tasks. Different types of prompts, including points, text, box, and mask prompts, are supported. The mask decoder comprises transformer layers with dynamic mask prediction heads and an Intersection-over-Union (IoU) score regression head. It maps the encoder embedding, prompt embeddings, and an output token to a mask. For user convenience, SAM offers a set of APIs with which segmentation masks can be obtained in just a few

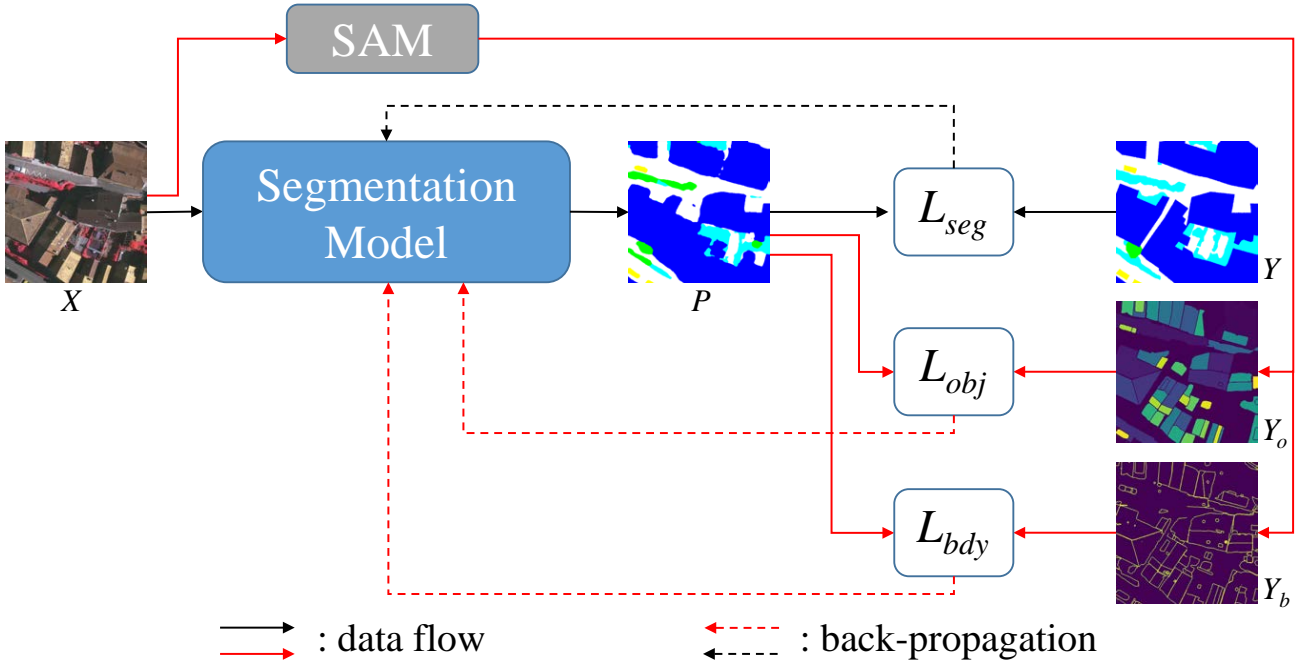


Fig. 2. The schematic diagram of the proposed method. The black arrows describe general semantic segmentation methods. The image X is fed into the segmentation model that generates the segmentation output P before the segmentation loss L_{seg} is computed by segmentation output and ground truth Y , which is used for back-propagation to update the model. The red arrows represent the processes we designed to leverage SGO and SGB. Two additional loss functions L_{obj} and L_{bdy} are computed by SGO Y_o and SGB Y_b that will also be used for model optimization together with L_{seg} . It should be noted that $P \in \mathbb{R}^{H \times W \times C}$ in this figure is the predicted score of the model for C classes. Here we take the category label corresponding to the maximum score of each pixel for visualization.

lines of code. Different segmentation mode options, i.e., fully automatic, bounding box, and point mode, are supported for different prompts in APIs.

Currently, SAM has made significant strides in diverse fields. In the realm of medical image processing, [35] introduced a straightforward image enhancement method by combining SAM-generated masks with raw images. Additionally, nnSAM [36] integrated the encoder of UNet with the pre-trained SAM encoder, harnessing the feature extraction capabilities of this large foundational vision model. Furthermore, [37, 38] delved into exploring SAM’s capacity to generate pseudo labels. Through these distinct technical approaches, these methods have propelled the application and development of SAM across various domains.

B. Segment Anything Model in Remote Sensing

The fundamental distinction between natural images and remote sensing images lies in their acquisition and context, encompassing factors such as acquisition methods, spectral and spatial resolutions, object scale and coverage, and content complexity [39, 40, 16]. SAMRS [28] introduced a prompt known as Rotated Bounding Box (R-Box) to guide SAM segmentation, subsequently generating a comprehensive remote sensing segmentation dataset. This groundbreaking work has paved the way for the integration of large-scale models and the utilization of big data in the field of remote sensing. On a parallel track, Text2Seg [29] devised a framework employing multiple foundational models to guide semantic segmentation of remote sensing images through text prompts.

However, prompt learning techniques explored in [27, 28, 29, 30, 31] necessitate careful selection based on the specific dataset characteristics, limiting the general applicability of SAM. Meanwhile, few-shot or zero-shot methods [24, 25, 26] demonstrate promising adaptability for remote sensing tasks, though their sensitivity to additional fine-tuning techniques remains a notable consideration [23]. More importantly, the absence of semantic information in SGO confines existing methods to binary classification tasks [24, 21, 30], or to multiple classification predictions via class-specific prompts [20, 19, 24], which undoubtedly limits the progression of SAM in remote sensing. In light of the aforementioned discussions, it is imperative to design an accessible and user-friendly framework for leveraging SGO and SGB in semantic segmentation tasks with multiple classes in remote sensing.

III. METHODOLOGY

The schematic diagram of the proposed framework is depicted in Fig. 2. In the conventional semantic segmentation task, the image is fed into the segmentation model to generate segmentation output, which is then used to calculate the segmentation loss. Subsequently, the model is updated based on the back-propagation algorithm, as depicted by the black arrows in Fig. 2. The additional steps introduced in our framework are highlighted by red arrows. Initially, we directly generate SGO and SGB using the SAM provided by Meta AI [18]. These outputs play a crucial role in computing the object loss and boundary loss, respectively, thereby contributing to the model’s training. In this section, we will provide detailed

explanations on SAM-Generation, network training, and the associated loss functions.

A. SAM-Generation

SAM provides a grid prompt technique to automatically process images. Given the input remote sensing image denote by $X \in \mathbb{R}^{H \times W \times 3}$, SAM can generate segmentation masks across the entire image at all plausible locations in the grid prompt setting [35]. In this study, we refer to the segmentation mask as the *object*, considering each segmentation mask as an individual enclosed region that can be regarded as an object. The generated objects are then stored into a list where we set a threshold of K to limit the maximum number of objects in X . Meanwhile, we also establish a threshold S to set a minimum limit on the number of pixels that a single object can contain, effectively filtering out very small segmentation masks. Consequently, a SAM-Generation object, denoted as SGO and represented by $Y_o \in \mathbb{R}^{H \times W}$ can be obtained, where the value of each pixel falls within the range of $[0, K]$. Pixels not segmented as objects, as well as boundaries, are assigned a value of 0, while the objects in Y_o are indexed by an identifier denoted as i , where $i \in [1, K]$. Concurrently, a boundary prior map is derived from SGO. This process involves outlining the exterior boundaries of each object within the list and merging these boundaries to produce a comprehensive boundary prior map, namely SGB, denoted by $Y_b \in \mathbb{R}^{H \times W}$. Unless specified otherwise, the boundaries in Y_b are set to 255, while others are set to 0 in the sequel. Visual examples of SGO and SGB are illustrated in Fig. 1 (c) and (d).

B. Network Training

The classical encoder-decoder networks, e.g., UNetformer [14], are widely used in semantic segmentation methods. In this work, we use them as the segmentation model in the proposed framework shown in Fig. 2. Given the input image X , the segmentation model produces the predicted segmentation output denote by $P \in \mathbb{R}^{H \times W \times C}$ where C is the number of categories of ground objects. The learning objective is to minimize the following cross entropy-based segmentation loss with respect to the parameters of segmentation model:

$$L_{seg} = - \sum_{\mathcal{H}, \mathcal{W}} \sum_{c \in C} Y^{(\mathcal{H}, \mathcal{W}, c)} \log(P^{(\mathcal{H}, \mathcal{W}, c)}), \quad (1)$$

where Y stands for the ground truth.

Given that SGO and SGB are solely utilized for computing loss functions, the proposed framework requires no additional modifications or adjustments to the network and training strategies. Thus, the learning objective for our method is to minimize the following composite loss function:

$$L_{total} = L_{seg} + \lambda_o L_{obj} + \lambda_b L_{bdy}, \quad (2)$$

where L_{obj} and L_{bdy} stand for the object loss and boundary loss, respectively, while λ_o and λ_b are two weighting coefficients to balance them.

1) *Object Loss*: The object loss is designed to maintain pixel consistency within the objects in a given input image. Given the input X , the output of the segmentation model is denoted as P . To compute the object loss, we iterate through all the objects in Y_o in order of id i . For each object, we first extract its mask M^i , i.e. the region in Y_o where the pixel value equals i . The object feature is then obtained by:

$$F_o^i = P \odot M^i, \quad (3)$$

where \odot stands for the Hadamard product. The object feature F_o^i denotes the model prediction filtered based on the area of the i -th object. Next, we can calculate the average feature of the object as:

$$F_{avg}^i = \frac{\mathcal{G}(F_o^i)}{N^i + 1} \odot M^i, \quad (4)$$

where \mathcal{G} calculates the sum of all pixels in the spatial dimension and reshapes to its original shape while N^i is the number of points in the i -th object. An extra one is added to avoid the denominator being zero. F_{avg}^i represents the expected mean value of all the pixels in the i -th object, thereby we can compute the object loss L_{obj} for all objects as:

$$L_{obj} = \sum_{i=1}^K \mathcal{MSE}(F_o^i, F_{avg}^i), \quad (5)$$

where \mathcal{MSE} is the mean squared error function.

Clearly, the proposed L_{obj} directly leverages the semantically meaningless regions generated by SAM, fully utilizing the detailed segmentation mask information in SGO.

2) *Boundary Loss*: Previous studies [41, 42, 33] have demonstrated that incorporating edge constraints can effectively enhance the performance of segmentation models in remote sensing tasks. Our observations indicate that SGO inherently contains highly detailed boundary information, as depicted in Fig. 1 (d). To leverage this boundary information, we set the boundary to 0 in Y_o and generate SGB, denoted as Y_b . In this work, the boundary metric (BF_1) [33], capable of directly computing boundary loss from the segmentation output P of the semantic model, is employed to evaluate the precision of boundary detection. The boundary loss L_{bdy} is given by:

$$L_{bdy} = 1 - BF_1, \quad (6)$$

where BF_1 is defined as:

$$BF_1 = 2 * \frac{p_b r_b}{p_b + r_b}, \quad (7)$$

with p_b and r_b being the precision and recall of the boundary that can comprehensively evaluate the accuracy of the boundary detection results from P and Y_b [33].

Finally, the overall objective function employed in training the segmentation model is given by Eq. (2), which sums the semantic segmentation loss L_{seg} , the object loss L_{obj} , and the boundary loss L_{bdy} .

IV. EXPERIMENTS AND DISCUSSION

A. Datasets

1) *ISPRS Vaihingen*: The ISPRS Vaihingen dataset comprises 16 true orthophotos with very high-resolution, averaging 2500×2000 pixels. Each orthophoto encompasses three channels, namely Near-Infrared, Red, and Green (NIRRG) of 9 cm ground sampling distance. This dataset includes five foreground classes, namely *impervious surface*, *building*, *low vegetation*, *tree*, *car*, and one background class (*clutter*). The 16 orthophotos are divided into a training set of 12 patches, and a test set of 4 patches. The training set comprises orthophotos of index numbers 1, 3, 23, 26, 7, 11, 13, 28, 17, 32, 34, 37, while the test set 5, 21, 15, 30.

2) *LoveDA Urban*: The LoveDA dataset contains two scenes, namely Urban and Rural. Considering the diverse distribution of ground objects, we selected the LoveDA Urban scene for our experiments. The LoveDA Urban comprises 1833 high-resolution optical remote sensing images, each with the size of 1024×1024 pixels. The images provide three channels, namely Red, Green, and Blue (RGB), with a ground sampling distance (GSD) of 30 cm. The dataset encompasses seven landcover categories, including *background*, *building*, *road*, *water*, *barren*, *forest*, and *agriculture* [43]. These images were collected from three cities (Nanjing, Changzhou, and Wuhan) in China. The 1833 images are divided into two parts, with 1156 images for training and 677 images for testing. Specifically, the training set contains images indexed from 1366 to 2521, while the test set spans images from 3514 to 4190.

The two datasets differ in sampling resolution, ground object categories, and label accuracy. Notably, the ISPRS Vaihingen exhibits higher sampling accuracy, a reduced number of categories, and more precise ground truth. In contrast, the LoveDA Urban presents the opposite characteristics. Conducting experiments on both datasets provides substantial evidence regarding the effectiveness of our framework. Throughout the training and testing processes, a sliding window is employed for dynamically assembling training batches, enabling the processing of large images without pre-splitting. The sliding window size is set at 256×256 , with a stride of 256 during training and an adjusted stride of 32 during testing. The use of a smaller stride in testing effectively mitigates border effects by averaging the prediction outcomes within overlapping regions [44, 45].

B. Evaluation Metrics

To assess the segmentation performance of the proposed framework, the mean F1 score (mF1) and the mean Intersection over Union (mIoU) are employed in our experiments. These widely used statistical indices allow for fair comparisons between the performance of our method and state-of-the-art baseline methods. In particular, we compute mF1 and mIoU of the five foreground classes for the ISPRS Vaihingen. The class labeled as *Clutter* or *Background* is treated as a cluttered and sparse class, and thus, performance statistics are not calculated for either class [9, 17]. In the case of LoveDA Urban, all seven categories are considered in our experiments. F1 and

IoU metrics are computed for each class identified by the index c using the following formulas:

$$F1 = 2 * \frac{p_c r_c}{p_c + r_c}, \quad (8)$$

$$IoU = \frac{TP_c}{TP_c + FP_c + FN_c}, \quad (9)$$

where TP_c , FP_c , and FN_c are true positives, false positives, and false negatives for the c -th class, respectively. Furthermore, p_c and r_c are given by:

$$p_c = \frac{TP_c}{TP_c + FP_c}, \quad (10)$$

$$r_c = \frac{TP_c}{TP_c + FN_c}. \quad (11)$$

Upon computing F1 and IoU for the main classes according to the definitions above, we derive their mean values, denoted as mF1 and mIoU, respectively.

C. Implementation details

The experiments were conducted using PyTorch on a single NVIDIA GeForce RTX 4090 GPU equipped with 24GB RAM. To generate SGO and SGB, we utilize the interface offered by Meta AI, which involves three pertinent parameters, namely “crop_nms_thresh”, “box_nms_thresh”, and “pred_iou_thresh” whose definitions can be found in Meta AI documentation¹. In our experiments, these values were configured to 0.5, 0.5, and 0.96, respectively. Note that a higher “pred_iou_thresh” value tends to generate more dependable raw output. Stochastic gradient descent (SGD) was employed as the optimization algorithm for training all models. Furthermore, the experiments employed a learning rate of 0.01, a momentum of 0.9, a decaying coefficient of 0.0005, and a batch size of 10. The values of λ_o and λ_b are set to 1.0 and 0.1, respectively.

Simple data augmentations, such as random rotation and flipping, were utilized. In addition, UNetformer [14], which benefits from its seamless integration of both CNN and transformer encoders, was employed as our baseline. This choice allows us to validate our approach across different classical networks. Specifically, the former utilizes ResNet (ResNet-18) [6] as its backbone, while the latter employs the Swin Transformer (SwinTrans-base) [46].

D. Performance Comparison

We benchmarked the performance of the proposed framework on two representative backbones, namely ResNet-18 and SwinTrans-base. The quantitative results are listed in Table I and Table II.

¹Meta AI: https://github.com/facebookresearch/segment-anything/tree/main/segment_anything

TABLE I
EXPERIMENTAL RESULTS ON THE ISPRS VAIHINGEN DATASET. WE PRESENT THE OA OF FIVE FOREGROUND CLASSES AND THREE OVERALL PERFORMANCE METRICS. ACCURACY OF EACH CATEGORY IS PRESENTED IN THE F1/IOU FORM. BOLD VALUES ARE THE BEST.

Method	Backbone	impervious surface	building	low vegetation	tree	car	mF1	mIoU
baseline	ResNet-18	92.33/85.76	96.25/92.78	80.47/67.33	90.85/83.22	89.35/80.75	89.85	81.97
Ours	ResNet-18	92.79/86.54	96.74/93.69	80.85/67.86	91.17/83.77	90.43/82.53	90.40	82.88
baseline	SwinTrans-base	93.41/87.64	96.92/94.02	81.53/68.82	90.91/83.33	88.46/79.31	90.24	82.62
Ours	SwinTrans-base	93.73/88.20	97.19/94.53	81.77/69.16	91.62/84.53	91.09/83.64	91.08	84.01

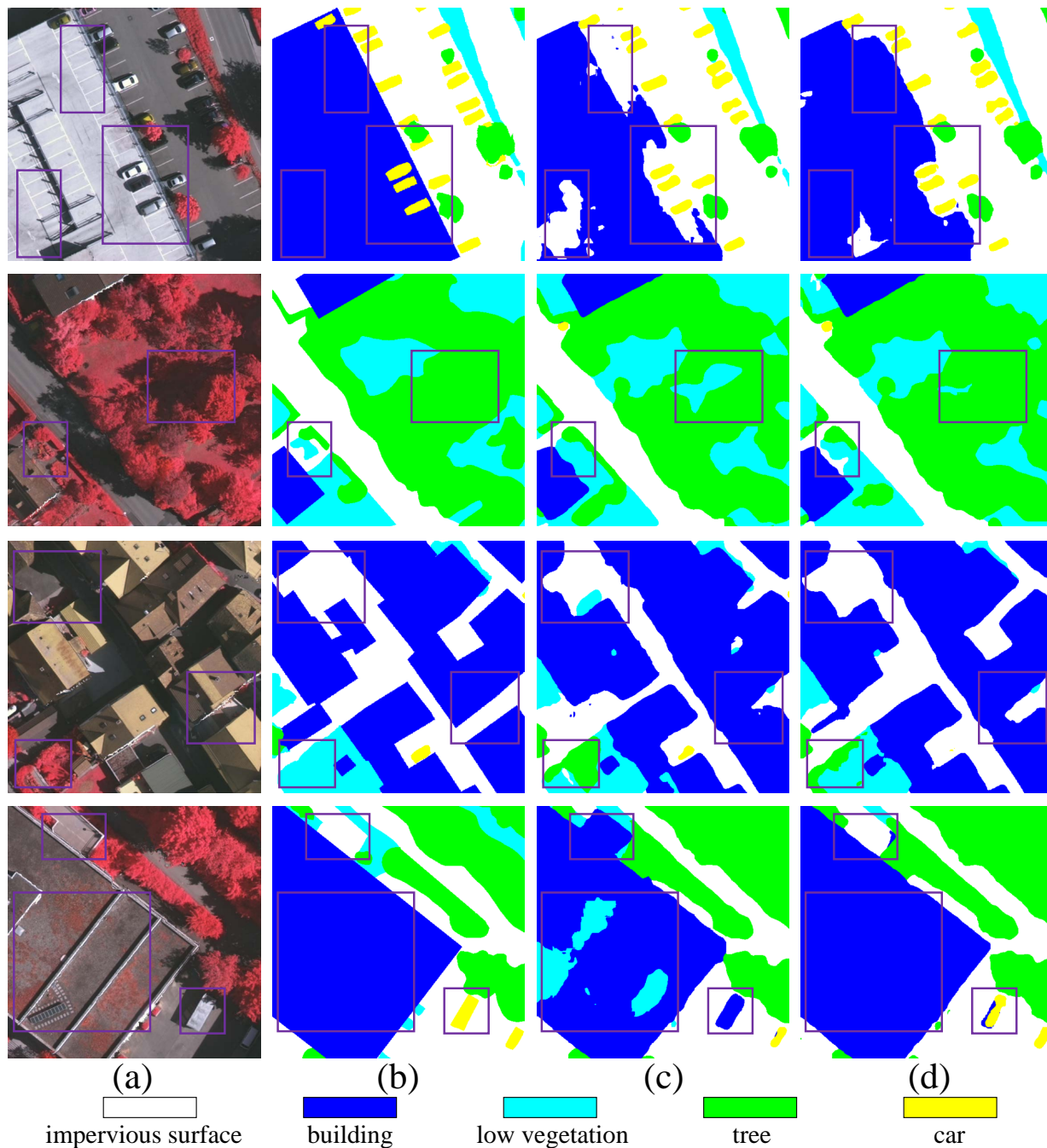


Fig. 3. Qualitative performance comparisons on the ISPRS Vaihingen with the size of 512×512 . (a) NIRRG images, (b) Ground truth, (c) baseline, (d) Ours. The first two rows show the results on ResNet-18 while the last two rows show the results on SwinTrans-base. Some purple boxes are added to highlight the differences.

TABLE II
EXPERIMENTAL RESULTS ON THE LOVE2D Urban DATASET. WE PRESENT THE OA OF FIVE FOREGROUND CLASSES AND THREE OVERALL PERFORMANCE METRICS. ACCURACY OF EACH CATEGORY IS PRESENTED IN THE F1/IOU FORM. BOLD VALUES ARE THE BEST.

Method	Backbone	background	building	road	water	barren	forest	agriculture	mF1	mIoU
baseline	ResNet-18	54.66/37.61	69.09/52.78	68.33/51.89	77.66/63.47	56.98/39.84	51.01/34.23	20.54/11.44	65.34	49.12
Ours	ResNet-18	55.43/38.34	75.91/61.17	73.61/58.24	80.55/67.43	43.19/27.55	57.05/39.91	43.64/27.91	65.74	50.55
baseline	SwinTrans-base	55.38/38.30	75.46/61.21	75.29/60.38	75.81/61.04	40.83/25.65	54.10/37.08	40.32/25.25	64.95	49.71
Ours	SwinTrans-base	56.40/39.27	77.23/62.91	74.74/59.67	77.30/63.00	44.44/28.57	53.30/36.33	44.17/28.34	66.02	50.68

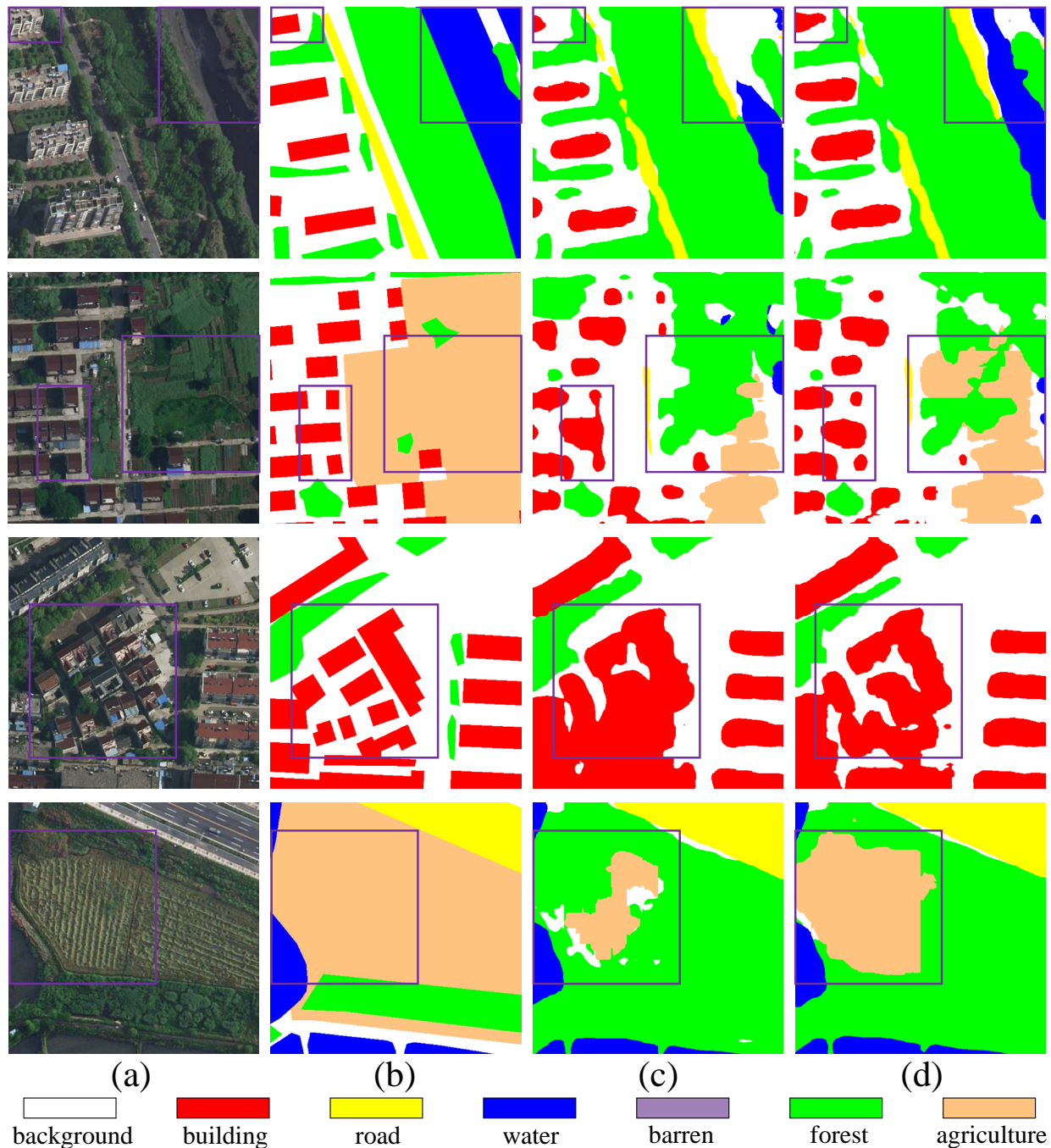


Fig. 4. Qualitative performance comparisons on the Love2D Urban with the size of 512×512 . (a) RGB images, (b) Ground truth, (c) baseline, (d) Ours. The first two rows show the results on ResNet-18 while the last two rows show the results on SwinTrans-base. Some purple boxes are added to highlight the differences.

1) *Performance Comparison on the Vaihingen dataset:* As indicated in Table I, our proposed framework demonstrates significant improvements in terms of both mF1 and mIoU metrics as compared to the baseline method. These results affirm the effectiveness of our approach in robustly capturing object and boundary representations. Notably, the incorporation of SGO and SGB information substantially enhances semantic segmentation performance in remote sensing images. When compared to the baseline, our method outperformed across all five classes, namely *impervious surface*, *building*, *low vegetation*, *tree*, and *car*. In particular, on the ISPRS Vaihingen dataset, ours (ResNet-18) achieved performance improvement of 1.08% and 1.78% in F1 and IoU, respectively, on the *Car* class as compared to baseline. Furthermore, the classification accuracy for *building* was enhanced by 0.49% and 0.91% in F1 and IoU, respectively, compared to the baseline. These improvements can be attributed to the inherent characteristics of *car* and *building* classes, which typically exhibit simpler and more standardized shapes compared to other ground object categories. For example, a car often presents a fixed-size rectangular shape under consistent sampling conditions, while a building typically manifests as a changing-size rectangle. As a result, SGO and SGB provide more reliable criteria for these specific categories, facilitating more accurate segmentation.

In contrast, *impervious surface*, *low vegetation*, and *tree* often feature intricate boundaries and varying sizes. Despite their complexity, SGO and SGB still offer valuable supplementary information for these specific categories. For instance, the classification accuracy for *impervious surface* was improved by 0.46% and 0.78% in F1 and IoU, respectively. Meanwhile, both *low vegetation* and *tree* showed comparable improvements in F1 and IoU metrics, reflecting their similar characteristics. In terms of overall performance, our model achieved an mF1 score of 90.40% and an mIoU of 82.88%, representing an increase of 0.55% and 0.91% compared to the baseline, respectively.

Our experiments with SwinTrans-base further substantiated our observations above. Specifically, our model (SwinTrans-base) demonstrated significant enhancements, exhibiting a notable 2.63% and 4.33% improvement in F1 and IoU metrics, respectively, for the *Car* class compared to the baseline. Moreover, we observed a slight increase in classification accuracy for the *building*, with improvements of 0.27% and 0.51% in F1 and IoU, respectively. In particular, the *tree* category exhibits a notable improvement, while the improvement in the *low vegetation* category is somewhat diminished, primarily due to their significant similarity. The overall performance corresponds to an mF1 score of 91.08% and an mIoU of 84.01%, marking respective increases of 0.84% and 1.39% compared to the baseline. These outcomes affirm that our proposed framework, with the aid of SGO and SGB across various models, achieved superior generalization performance.

Fig. 3 presents a visual comparison between the results produced by the baseline method and our approach. Throughout all subfigures, purple boxes highlight areas of interest. Firstly, our method excelled in precisely segmenting entire objects, notably evident in the clear delineation of *building* shown in the first and fourth rows. Secondly, our approach significantly

refined object boundaries, as seen *low vegetation* in the second row and the *building* in the third row, aligning more closely with the actual ground truth boundaries. Furthermore, our method successfully addressed the segmentation of challenging categories, such as *tree* in the second row, *building* in the third row, and *impervious surface* and *car* in the fourth row. These improvements primarily stem from the object region and boundary details contained in the SGO and SGB. Leveraging the well-designed framework founded on object and boundary loss functions allows for the comprehensive exploitation of this detailed information, leading to the observed improvements in segmentation accuracy.

2) *Performance Comparison on the LoveDA Urban:* Experiments conducted on the LoveDA Urban dataset yielded results similar to those observed in the ISPRS Vaihingen dataset, despite variations in sampling resolution and ground object categories between the two datasets. As shown in Table II, the classification accuracy for *building*, *water*, and *agriculture* were 75.91%/61.17%, 80.55%/67.43%, and 43.64%/27.91%, respectively, which amounts to an increase of 6.82%/8.39%, 2.89%/3.96%, and 23.1%/16.47% in F1 and IoU, respectively, as compared to the baseline (ResNet-18). Meanwhile, our findings with SwinTrans-base consistently confirmed advantages for these classes characterized by regular shapes and uncomplicated borders. The corresponding mF1 and mIoU values were 65.74%, 50.55% respectively, marking increases of 0.4%, and 1.43%, respectively, over baseline (ResNet-18) while the increases for mF1 and mIoU on SwinTrans-base were 1.07%, 0.97%.

However, upon evaluating this dataset, we observed fluctuating performance changes when comparing the results of the two networks. ResNet-18 exhibited improved performance for *road* and *forest*, whereas SwinTrans-base demonstrated the opposite trend. Conversely, the performance for *barren* decreased in ResNet-18 but improved in SwinTrans-base. The primary reason for this discrepancy is that these three categories have intricate boundaries and varying sizes. Notably, the proportion of *barren* is very small, leading to volatility in its results during the experiments [43]. While the segmentation model aims to enhance overall performance, it cannot guarantee consistent improvement in every category. Nevertheless, the overall performance improvement of our framework demonstrates the instructive nature of this approach for subsequent works.

Fig. 4 presents a visualization example from the LoveDA Urban, with purple boxes highlighting areas of interest in all subfigures. Firstly, the model demonstrated enhanced accuracy in identifying *building*, evident across the first, second, and third rows. Furthermore, a more complete identification of *water* and *agriculture* objects was apparent, exemplified by the *water* in the first row and *agriculture* in the second and fourth rows. These observations closely align with the improvements indicated by the mF1 and mIoU metrics as presented in Table II.

E. Ablation Study

To emphasize the distinct roles of the two loss functions in the proposed framework, we conducted ablation experiments

TABLE III

ABLATION STUDIES ON THE ISPRS VAIHINGEN DATASET. ACCURACY OF EACH CATEGORY IS PRESENTED IN THE F1/IOU FORM. BOLD VALUES ARE THE BEST.

Method	impervious surface	building	low vegetation	tree	car	mF1	mIoU
L_{seg}	92.33/85.76	96.25/92.78	80.47/67.33	90.85/83.22	89.35/80.75	89.85	81.97
$L_{seg} + L_{obj}$	92.55/86.14	96.48/93.20	80.76/67.73	91.14/83.72	89.91/81.67	90.17	82.49
$L_{seg} + L_{bdy}$	92.79/86.54	96.79/93.78	80.66/67.59	90.94/83.38	89.49/80.99	90.13	82.45
$L_{seg} + L_{obj} + L_{bdy}$	92.79/86.54	96.74/93.69	80.85/67.86	91.17/83.77	90.43/82.53	90.40	82.88

TABLE IV

ABLATION STUDIES ON THE LOVE DA URBAN DATASET. ACCURACY OF EACH CATEGORY IS PRESENTED IN THE F1/IOU FORM. BOLD VALUES ARE THE BEST.

Method	background	building	road	water	barren	forest	agriculture	mF1	mIoU
L_{seg}	54.66/37.61	69.09/52.78	68.33/51.89	77.66/63.47	56.98/39.84	51.01/34.23	20.54/11.44	65.34	49.12
$L_{seg} + L_{obj}$	53.04/36.08	72.54/56.91	71.68/55.86	75.62/60.79	54.76/37.70	61.00/43.89	23.50/13.32	65.53	49.47
$L_{seg} + L_{bdy}$	55.49/38.39	72.73/57.15	73.30/57.86	79.33/65.74	48.54/32.05	54.54/37.49	41.13/25.89	65.88	50.24
$L_{seg} + L_{obj} + L_{bdy}$	55.43/38.34	75.91/61.17	73.61/58.24	80.55/67.43	43.19/27.55	57.05/39.91	43.64/27.91	65.74	50.55

using ResNet-18 on two datasets, as detailed in Table III and Table IV. The results underscore that the independent use of these two loss functions enhanced the overall performance of the segmentation model, validating the value and efficacy of SAM’s raw output. When examining the results on *impervious surface* and *building* of the ISPRS Vaihingen dataset, it is evident that only the boundary loss exhibited comparable improvement as compared to the combined loss. This suggests that in specific tasks, such as building detection, SAM-Generation results can be fully explored using only the boundary loss. However, in semantic segmentation tasks, where various ground objects possess highly complex boundaries, leveraging both SGO and SGB to their fullest extent becomes necessary. Furthermore, the results of these two loss functions on different categories, as listed in Table III and Table IV, highlight the disparate behaviors exhibited across various categories. By combining the object and boundary loss functions, we proposed a versatile and streamlined framework for directly leveraging SGO and SGB, showcasing robust generalization capabilities in remote sensing image semantic segmentation tasks.

V. CONCLUSION

This work proposed a simple and versatile framework designed to fully exploit the raw output of SAM in conjunction with a segmentation model. Acknowledging the distinctions between remote sensing images and natural images, as well as the characteristics of SGO and SGB, we developed an auxiliary optimization strategy by exploiting two novel loss functions, namely the object loss and the boundary loss. This strategy facilitates improvements in fundamental semantic segmentation tasks without requiring additional network modules. Notably, our introduction of object loss, motivated by the consistency of objects, represents the initial loss function capable of directly utilizing SGO without semantic information. Our validation conducted on two publicly available datasets underscores the robust performance of our framework. Finally, it is worth emphasizing that this work has initiated a preliminary exploration of SAM’s raw output, revealing the potential for large models such as SAM in the field of remote sensing.

REFERENCES

- [1] Q. Yuan, H. Shen, T. Li, Z. Li, S. Li, Y. Jiang, H. Xu, W. Tan, Q. Yang, J. Wang *et al.*, “Deep learning in environmental remote sensing: Achievements and challenges,” *Remote Sensing of Environment*, vol. 241, p. 111716, 2020.
- [2] R. Li, S. Zheng, C. Duan, L. Wang, and C. Zhang, “Land cover classification from remote sensing images based on multi-scale fully convolutional network,” *Geo-spatial information science*, vol. 25, no. 2, pp. 278–294, 2022.
- [3] A. Gupta, S. Watson, and H. Yin, “Deep learning-based aerial image segmentation with open data for disaster impact assessment,” *Neurocomputing*, vol. 439, pp. 22–33, 2021.
- [4] S. Khan, K. Muhammad, T. Hussain, J. Del Ser, F. Cuzzolin, S. Bhattacharyya, Z. Akhtar, and V. H. C. de Albuquerque, “DeepSmoke: Deep learning model for smoke detection and segmentation in outdoor environments,” *Expert Systems with Applications*, vol. 182, p. 115125, 2021.
- [5] O. Ronneberger, P. Fischer, and T. Brox, “U-Net: Convolutional networks for biomedical image segmentation,” in *Medical Image Computing and Computer-Assisted Intervention—MICCAI 2015: 18th International Conference, Munich, Germany, October 5–9, 2015, Proceedings, Part III 18*. Springer, 2015, pp. 234–241.
- [6] K. He, X. Zhang, S. Ren, and J. Sun, “Deep residual learning for image recognition,” in *Proceedings of the IEEE conference on computer vision and pattern recognition*, 2016, pp. 770–778.
- [7] A. Vaswani, N. Shazeer, N. Parmar, J. Uszkoreit, L. Jones, A. N. Gomez, Ł. Kaiser, and I. Polosukhin, “Attention is all you need,” *Advances in neural information processing systems*, vol. 30, 2017.
- [8] A. Dosovitskiy, L. Beyer, A. Kolesnikov, D. Weissenborn, X. Zhai, T. Unterthiner, M. Dehghani, M. Minderer, G. Heigold, S. Gelly *et al.*, “An image is worth 16x16 words: Transformers for image recognition at scale,” *arXiv preprint arXiv:2010.11929*, 2020.
- [9] F. I. Diakogiannis, F. Waldner, P. Caccetta, and C. Wu, “ResUNet-a: A deep learning framework for semantic segmentation of remotely sensed data,” *ISPRS Journal of Photogrammetry and Remote Sensing*, vol. 162, pp. 94–114, 2020.
- [10] C. Hazirbas, L. Ma, C. Domokos, and D. Cremers, “FuseNet: Incorporating depth into semantic segmentation via fusion-based CNN architecture,” in *Asian conference on computer vision*, 2016, pp. 213–228.
- [11] D. Hong, J. Yao, D. Meng, Z. Xu, and J. Chanussot, “Multi-modal GANs: Toward crossmodal hyperspectral–multispectral image segmentation,” *IEEE Transactions on Geoscience and Remote Sensing*, vol. 59, no. 6, pp. 5103–5113, 2020.
- [12] L. Wang, R. Li, C. Duan, C. Zhang, X. Meng, and S. Fang,

- “A novel transformer based semantic segmentation scheme for fine-resolution remote sensing images,” *IEEE Geoscience and Remote Sensing Letters*, vol. 19, pp. 1–5, 2022.
- [13] Z. Xu, W. Zhang, T. Zhang, Z. Yang, and J. Li, “Efficient transformer for remote sensing image segmentation,” *Remote Sensing*, vol. 13, no. 18, p. 3585, 2021.
- [14] L. Wang, R. Li, C. Zhang, S. Fang, C. Duan, X. Meng, and P. M. Atkinson, “UNetFormer: A UNet-like transformer for efficient semantic segmentation of remote sensing urban scene imagery,” *ISPRS Journal of Photogrammetry and Remote Sensing*, vol. 190, pp. 196–214, 2022.
- [15] C. Zhang, W. Jiang, Y. Zhang, W. Wang, Q. Zhao, and C. Wang, “Transformer and CNN hybrid deep neural network for semantic segmentation of very-high-resolution remote sensing imagery,” *IEEE Transactions on Geoscience and Remote Sensing*, vol. 60, pp. 1–20, 2022.
- [16] X. Ma, X. Zhang, Z. Wang, and M.-O. Pun, “Unsupervised domain adaptation augmented by mutually boosted attention for semantic segmentation of VHR remote sensing images,” *IEEE Transactions on Geoscience and Remote Sensing*, vol. 61, pp. 1–15, 2023.
- [17] H. Wu, P. Huang, M. Zhang, W. Tang, and X. Yu, “CMTFNet: CNN and multiscale transformer fusion network for remote sensing image semantic segmentation,” *IEEE Transactions on Geoscience and Remote Sensing*, 2023.
- [18] A. Kirillov, E. Mintun, N. Ravi, H. Mao, C. Rolland, L. Gustafson, T. Xiao, S. Whitehead, A. C. Berg, W.-Y. Lo *et al.*, “Segment anything,” *arXiv preprint arXiv:2304.02643*, 2023.
- [19] S. Ren, F. Luzzi, S. Lahrichi, K. Kassaw, L. M. Collins, K. Bradbury, and J. M. Malof, “Segment anything, from space?” *arXiv preprint arXiv:2304.13000*, 2023.
- [20] L. Stearns, C. van der Veen, and S. Shankar, “Segment anything in glaciology: An initial study implementing the segment anything model (SAM),” 2023.
- [21] L. Ding, K. Zhu, D. Peng, H. Tang, and H. Guo, “Adapting segment anything model for change detection in HR remote sensing images,” *arXiv preprint arXiv:2309.01429*, 2023.
- [22] C. Zhang, P. Marfatia, H. Farhan, L. Di, L. Lin, H. Zhao, H. Li, M. D. Islam, and Z. Yang, “Enhancing USDA NASS cropland data layer with segment anything model,” in *2023 11th International Conference on Agro-Geoinformatics (Agro-Geoinformatics)*. IEEE, 2023, pp. 1–5.
- [23] L. P. Osco, Q. Wu, E. L. de Lemos, W. N. Gonçalves, A. P. M. Ramos, J. Li, and J. M. Junior, “The segment anything model (SAM) for remote sensing applications: From zero to one shot,” *International Journal of Applied Earth Observation and Geoinformation*, vol. 124, p. 103540, 2023.
- [24] X. Li, C. Wen, Y. Hu, and N. Zhou, “RS-CLIP: Zero shot remote sensing scene classification via contrastive vision-language supervision,” *International Journal of Applied Earth Observation and Geoinformation*, vol. 124, p. 103497, 2023.
- [25] X. Qi, Y. Wu, Y. Mao, W. Zhang, and Y. Zhang, “Self-guided few-shot semantic segmentation for remote sensing imagery based on large vision models,” *arXiv preprint arXiv:2311.13200*, 2023.
- [26] M. M. Al Rahhal, Y. Bazi, H. Elgibreen, and M. Zuair, “Vision-language models for zero-shot classification of remote sensing images,” *Applied Sciences*, vol. 13, no. 22, p. 12462, 2023.
- [27] K. Chen, C. Liu, H. Chen, H. Zhang, W. Li, Z. Zou, and Z. Shi, “RSPrompter: Learning to prompt for remote sensing instance segmentation based on visual foundation model,” *arXiv preprint arXiv:2306.16269*, 2023.
- [28] D. Wang, J. Zhang, B. Du, M. Xu, L. Liu, D. Tao, and L. Zhang, “SAMRS: Scaling-up remote sensing segmentation dataset with segment anything model,” in *Thirty-seventh Conference on Neural Information Processing Systems Datasets and Benchmarks Track*, 2023.
- [29] J. Zhang, Z. Zhou, G. Mai, L. Mu, M. Hu, and S. Li, “Text2Seg: Remote sensing image semantic segmentation via text-guided visual foundation models,” *arXiv preprint arXiv:2304.10597*, 2023.
- [30] R. I. Sultan, C. Li, H. Zhu, P. Khanduri, M. Brocanelli, and D. Zhu, “GeoSAM: Fine-tuning SAM with sparse and dense visual prompting for automated segmentation of mobility infrastructure,” *arXiv preprint arXiv:2311.11319*, 2023.
- [31] S. Julka and M. Granitzer, “Knowledge distillation with segment anything (SAM) model for planetary geological mapping,” *arXiv preprint arXiv:2305.07586*, 2023.
- [32] X. Zhao, W. Ding, Y. An, Y. Du, T. Yu, M. Li, M. Tang, and J. Wang, “Fast segment anything,” *arXiv preprint arXiv:2306.12156*, 2023.
- [33] A. Bokhovkin and E. Burnaev, “Boundary loss for remote sensing imagery semantic segmentation,” in *International Symposium on Neural Networks*. Springer, 2019, pp. 388–401.
- [34] I. Markus Gerke, “Use of the stair vision library within the ISPRS 2D semantic labeling benchmark (Vaihingen),” *Use of the stair vision library within the isprs 2d semantic labeling benchmark (vaihingen)*, 2014.
- [35] Y. Zhang, T. Zhou, P. Liang, and D. Z. Chen, “Input augmentation with SAM: Boosting medical image segmentation with segmentation foundation model,” *arXiv preprint arXiv:2304.11332*, 2023.
- [36] Y. Li, B. Jing, X. Feng, Z. Li, Y. He, J. Wang, and Y. Zhang, “nnSAM: Plug-and-play segment anything model improves nnUNet performance,” *arXiv preprint arXiv:2309.16967*, 2023.
- [37] P.-T. Jiang and Y. Yang, “Segment anything is a good pseudo-label generator for weakly supervised semantic segmentation,” *arXiv preprint arXiv:2305.01275*, 2023.
- [38] Z. Huang, H. Liu, H. Zhang, F. Xing, A. Laine, E. Angelini, C. Hendon, and Y. Gan, “Push the boundary of SAM: A pseudo-label correction framework for medical segmentation,” *arXiv preprint arXiv:2308.00883*, 2023.
- [39] J. Li, X. Huang, and J. Gong, “Deep neural network for remote-sensing image interpretation: Status and perspectives,” *National Science Review*, vol. 6, no. 6, pp. 1082–1086, 2019.
- [40] Z. Zheng, Y. Zhong, J. Wang, and A. Ma, “Foreground-aware relation network for geospatial object segmentation in high spatial resolution remote sensing imagery,” in *Proceedings of the IEEE/CVF conference on computer vision and pattern recognition*, 2020, pp. 4096–4105.
- [41] D. Marmanis, K. Schindler, J. D. Wegner, S. Galliani, M. Datcu, and U. Stilla, “Classification with an edge: Improving semantic image segmentation with boundary detection,” *ISPRS Journal of Photogrammetry and Remote Sensing*, vol. 135, pp. 158–172, 2018.
- [42] S. Liu, W. Ding, C. Liu, Y. Liu, Y. Wang, and H. Li, “ERN: Edge loss reinforced semantic segmentation network for remote sensing images,” *Remote Sensing*, vol. 10, no. 9, p. 1339, 2018.
- [43] J. Wang, Z. Zheng, A. Ma, X. Lu, and Y. Zhong, “LoveDA: A remote sensing land-cover dataset for domain adaptive semantic segmentation,” in *Proceedings of the Neural Information Processing Systems Track on Datasets and Benchmarks*, vol. 1, 2021, pp. 1–17.
- [44] N. Audebert, B. Le Saux, and S. Lefèvre, “Beyond RGB: Very high resolution urban remote sensing with multimodal deep networks,” *ISPRS journal of photogrammetry and remote sensing*, vol. 140, pp. 20–32, 2018.
- [45] X. Ma, X. Zhang, and M.-O. Pun, “A crossmodal multiscale fusion network for semantic segmentation of remote sensing data,” *IEEE Journal of Selected Topics in Applied Earth Observations and Remote Sensing*, vol. 15, pp. 3463–3474, 2022.
- [46] Z. Liu, Y. Lin, Y. Cao, H. Hu, Y. Wei, Z. Zhang, S. Lin, and B. Guo, “Swin transformer: Hierarchical vision transformer using shifted windows,” in *Proceedings of the IEEE/CVF international conference on computer vision*, 2021, pp. 10012–10022.